Controlling spins with surface magnon polaritons

Jamison Sloan,[1,*,†] Nicholas Rivera,[2,*] John D. Joannopoulos,[2] Ido Kaminer,[3] and Marin Soljačić[2]
[1]*Research Laboratory of Electronics, Massachusetts Institute of Technology, Cambridge, Massachusetts 02139, USA*
[2]*Department of Physics, Massachusetts Institute of Technology, Cambridge, Massachusetts 02139, USA*
[3]*Department of Electrical Engineering, Technion—Israel Institute of Technology, Haifa 32000, Israel*

(Received 11 February 2019; revised manuscript received 11 November 2019; published 30 December 2019)

Polaritons in metals, semimetals, semiconductors, and polar insulators can allow for extreme confinement of electromagnetic energy, providing many promising opportunities for enhancing typically weak light-matter interactions such as multipolar radiation, multiphoton spontaneous emission, Raman scattering, and material nonlinearities. These extremely confined polaritons are quasielectrostatic in nature, with most of their energy residing in the electric field. As a result, these "electric" polaritons are far from optimized for enhancing emission of a magnetic nature, such as spin relaxation, which is typically many orders of magnitude slower than corresponding electric decays. Here, we take concepts of "electric" polaritons into magnetic materials, and propose using surface magnon polaritons in *negative magnetic permeability* materials to strongly enhance spin relaxation in nearby emitters. Specifically, we provide quantitative examples with MnF_2 and FeF_2, enhancing spin transitions in the THz spectral range. We find that these magnetic polaritons in 100-nm thin films can be confined to lengths over 10 000 times smaller than the wavelength of a photon at the same frequency, allowing for a surprising 12 orders of magnitude enhancement in magnetic dipole transitions. This takes THz spin-flip transitions, which normally occur at timescales on the order of a year, and forces them to occur at sub-ms timescales. Our results suggest an interesting platform for polaritonics at THz frequencies, and more broadly, a way to use polaritons to control light-matter interactions.

DOI: 10.1103/PhysRevB.100.235453

Polaritons, collective excitations of light and matter, offer the ability to concentrate electromagnetic energy down to volumes far below that of a photon in free space [1–6], holding promise to achieve the long-standing goal of low-loss confinement of electromagnetic energy at the near-atomic scale. The most famous examples are surface plasmon polaritons on conductors, which arise from the coherent sloshing of surface charges accompanied by an evanescent electromagnetic field. These collective excitations are so widespread in optics that their manipulation is referred to as plasmonics. Plasmons enjoy a myriad of applications, particularly in spectroscopy due to their enhanced interactions with matter. This enhancement applies to spontaneous emission, Raman scattering, optical nonlinearities, and even dipole-"forbidden" transitions in emitters [7–16]. Beyond plasmons in metals, polaritons in polar dielectrics, such as phonon polaritons [17–20] are now being exploited for similar applications due to their ability to concentrate electromagnetic energy on the nanoscale in the mid-IR/THz spectral range.

The ability of nanoconfined polaritons to strongly enhance electromagnetic interactions with matter can ultimately be understood in terms of electromagnetic energy density. An electromagnetic quantum of energy $\hbar\omega$, confined to a volume V, leads to a characteristic root-mean-square electric field of order $\sqrt{\frac{\hbar\omega}{\epsilon_0 V}}$. In the case of field interaction with an electron in an emitter, this characteristic field drives spontaneous emission, and thus concentration of energy to smaller volumes leads to enhanced emission. This well-studied phenomenon is best known as the Purcell effect [21]. Interestingly, if one looks at the electromagnetic energy distribution of a highly confined plasmon or phonon polariton, one finds that an overwhelming majority of this energy resides in the electric field [22–24]. For a polariton with a wavelength 100 times smaller than that of a photon at the same frequency, the magnitude of E is then 100 times larger than that of $\mu_0 cH$. In sharp contrast to free space wave propagation, the energy residing in the magnetic field is of the order of a mere 0.01% of the total energy $\hbar\omega$. This largely suggests that such excitations are relatively inefficient for enhancing spontaneous emission processes which couple to the magnetic field, such as spin-flip transitions or magnetic multipole decays. As such, enabling magnetic decays at very fast rates represents a rewarding challenge, as increasing rates of spontaneous emission can provide opportunities for detectors, devices, and sources of light.

The Purcell enhancement of magnetic dipole transitions has been approached by a few basic means: The use of highly confined resonances at optical frequencies [25,26], metamaterials [27,28], and for microwave frequencies, materials with simultaneously very high quality factors and highly confined fields. These advances are reviewed in Ref. [29]. Many of these methods have the benefit of compatibility with well-known materials and use at optical frequencies, but the Purcell enhancements in these cases are typically very far from maximal Purcell enhancements that can be achieved with "electric" polaritons at similar frequencies [14,16,30–33]. This prompts the question: What kind of electromagnetic response allows one to achieve a similar degree of very strong enhancement for magnetic transitions?

*These authors contributed equally to this paper.
†Corresponding author: jamison@mit.edu

The duality between electric and magnetic phenomena, combined with ideas from plasmonics and nano-optics, suggests a pathway for achieving strong magnetic transition enhancement: Highly confined magnetic modes in materials with negative magnetic *permeability*. In particular, plasmon and phonon polaritons are associated with a negative dielectric permittivity $\epsilon(\omega)$. By the well-established principle of electromagnetic duality [34,35], if one replaces $\epsilon(\omega)$ with the magnetic permeability $\mu(\omega)$, then the electric field $\mathbf{E}$ in the dielectric structure becomes the magnetic field $\mathbf{H}$ in the dual magnetic structure. Thus, to very efficiently enhance magnetic decays, one desires a material with negative $\mu(\omega)$ which supports modes dual to "electric" surface polaritons. While likely not the only example, AFMR is a well-studied example of a phenomenon which can provide precisely this permeability, and the corresponding modes are surface magnon polaritons (SMPs) [36–38].

Here, we use macroscopic quantum electrodynamics (MQED) of magnetic materials to propose extreme enhancement of magnetic transitions in nearby quantum emitters by using highly confined SMPs. We find enhancement of spin relaxation rates by over 12 orders of magnitude, showing magnetic Purcell enhancements as large as the highest limits predicted for electric Purcell enhancements. We discuss how the losses present in magnetic materials impact the magnetic decay rate and argue that even with these considerations, extremely large enhancements can be achieved. Such enhancements could provide access to extremely fast magnetic dipole decays, shortening radiative lifetimes on the order of a year to submillisecond timescales.

The organization of this paper is as follows: In Sec. I, we review the classical electrodynamics of SMPs and derive the dispersion relation and mode profile of SMPs for the example of an antiferromagnetic thin film. We briefly review the propagation properties of these modes and, in particular, note their extremely large confinement. In Sec. II, we use MQED to quantize the SMP modes and calculate the spontaneous emission rate of nearby magnetic dipole emitters into these modes. Finally, in Sec. III, we provide quantitative results for the spontaneous emission by spin systems near existing magnon-polaritonic materials, such as MnF_2 and FeF_2.

I. SURFACE MAGNON POLARITON MODES

The spin interactions in solids which give rise to different varieties of magnetic order have been studied extensively. Of particular note for our purposes is the study of the long-range order established by spin waves in (anti)ferromagnets [39–47]. These spin waves can be excited at the level of a single quantum, and the quasiparticles associated with these excitations are magnons [37]. More recently, magnons have attracted considerable attention for their ability to interact with electric currents and electron spins, leading to the rapidly growing field of magnon spintronics [48–57].

We begin by reviewing the confined modes which exist on thin films of materials with negative magnetic permeability, denoted $\mu(\omega)$. The modes we describe are well-studied SMPs [36,58–60] with $\mathrm{Re}\,\mu(\omega) \leqslant 0$. At a microscopic level, the modes correspond to ordered precession of the spins in an antiferromagnetic lattice and are also referred to as surface spin waves [61]. The classical dynamics of spin-wave propagation are governed by the Landau-Lifshitz-Gilbert equation, which accounts for damping [62,63]. These microscopic interactions give rise to a magnetic susceptibility (or equivalently a magnetic permeability) which dictates how macroscopic electromagnetic fields propagate in the material. Given the classical solutions to the Maxwell equations in a material configuration, one can then quantize the magnon modes, allowing the use of quantum optics techniques to describe the interaction of magnon modes in the vicinity of emitters. We construct these classical solutions, quantize these modes, and then solve for magnetic dipole transition rates into these modes.

TABLE I. Anisotropy fields, exchange fields, sublattice magnetization, resonance frequencies, and damping constants (where known) for antiferromagnetic materials that can support SMPs. Parameters are taken from Refs. [66,69].

Material	$\mu_0 H_A(T)$	$\mu_0 H_E$ (T)	$\mu_0 H_M$ (T)	ω_0 (rad THz)	τ (nsec)
MnF_2	0.787	53.0	0.06	1.69	7.58
FeF_2	19.745	53.3	0.056	9.89	0.11
$GdAlO_3$	0.365	1.88	0.062	0.23	–

For the specific case of an antiferromagnetic material near resonance, the frequency-dependent permeability which includes material losses takes the form of a Lorentz oscillator which depends on the microscopic magnetic properties of the antiferromagnetic crystal. Studies of the crystal structures of important antiferromagnetic materials can be found in Ref. [64]. The magnetic permeability function for antiferromagnetic resonance (AFMR) in the absence of an external magnetizing field from [65–67] is

$$\mu_{xx} = \mu_{yy} = 1 + \frac{2\gamma^2 H_A H_M}{\omega_0^2 - (\omega + i\Gamma)^2}, \tag{1}$$

with coordinates shown in Fig. 1. In Eq. (1), ω_0 is the resonance frequency, H_A is the anisotropy field, H_M is the sublattice magnetization field, γ is the gyromagnetic ratio, and $\Gamma = 1/\tau$ is a phenomenological damping parameter inversely proportional to the loss relaxation time τ. Furthermore, in the approximation of low damping, the resonant frequency is given as $\omega_0 = \gamma\sqrt{2H_A(H_A + H_E)}$, where H_E is the exchange field which is representative of the magnetic field required to invert neighboring spin pairs. For antiferromagnetic materials such as MnF_2 and FeF_2, the resonance frequencies ω takes values 1.69×10^{12} and 9.89×10^{12} rad/s, respectively, and have negative permeability over a relatively narrow bandwidth on the scale of a few GHz. Most importantly for our purposes, $\mathrm{Re}\mu(\omega) < 0$ for $\omega < \omega_0 < \omega_{\max}$, which will permit surface-confined modes. Finally, we note that we have implicitly assumed that the magnetic permeability carries no dependence on the wave vector through nonlocal effects. For wavelengths which substantially exceed the atomic lattice spacing, this should be an excellent approximation. A more detailed discussion of nonlocality in terms of mean-field parameters from Landau-Ginzburg phase transition theory can be found in Ref. [68]. Table I shows values of material parameters for a variety of antiferromagnetic materials. Figure 2(a) shows the real and imaginary parts of the magnetic permeability $\mu(\omega)$

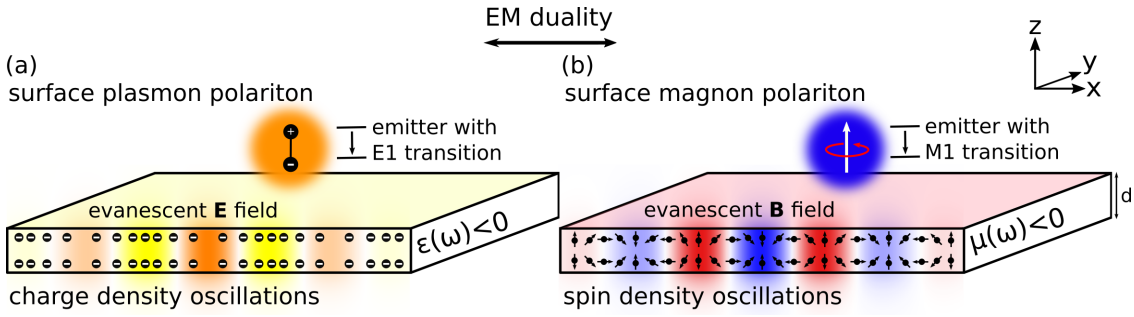

FIG. 1. Electromagnetically dual relationship between surface plasmon polaritons on negative permittivity materials and surface magnon polaritons on negative permeability materials. (a) Surface plasmon polariton represented as charge density oscillations in a negative ϵ material. These quantum fluctuations can couple strongly to an electric dipole emitter near the surface to drive enhanced spontaneous emission. (b) Surface magnon polariton represented as a spin density oscillation in a negative μ material. These quantum fluctuations can couple strongly to a magnetic dipole emitter near the surface to drive enhanced spontaneous emission. Both electric and magnetic surface polaritons can exhibit strong mode confinement, helping to overcome the mismatch between mode wavelength and emitter size.

associated with the AFMR in MnF_2. We see that at the peak of the resonance, $\mathrm{Re}(\mu) \approx -40$ and $\mathrm{Im}(\mu) \approx 90$.

We now discuss the geometry of the thin-film configurations we study. Antiferromagnetic fluorides exhibit a uniaxial permeability structure with two orthogonal components of the permeability tensor given by $\mu(\omega)$ above, and the other orthogonal component as unity. We start by focusing on crystal orientations in which $\mu = (\mu(\omega), \mu(\omega), 1)$. It is also worthwhile to note that experiments, specifically on nonreciprocal optical phenomena [70], have been performed on these materials in a less conventional geometry where $\mu = (\mu(\omega), 1, \mu(\omega))$. The in-plane anisotropy of this configuration substantially complicates the dispersion relation and propagation structure of the modes. As such, we focus primarily on the isotropic case but present results for the in-plane anisotropic case near the end of the text.

For concreteness, we focus on MnF_2, a material which has been studied in depth both in theory and experiment [71,72], and also exhibits a relatively low propagation loss. We note that FeF_2 is also a promising candidate with higher resonance frequency, but also higher loss [73,74]. We solve for SMPs supported by optically very thin (here, submicron thickness denoted by d) MnF_2 films surrounded by air. For the confined modes we consider, the effect of retardation is negligible [75], and thus we can find the magnon modes using a quasimagnetostatic treatment as described in Ref. [66]. In the magnetostatic limit, the resulting "polaritons" are much more magnonlike than photonlike. Nevertheless, many of the applications which are considered in polaritonics are feasible with these modes [2,4]. In the absence of retardation, the electric field is negligible, and the magnetic field, since there are no free currents, satisfies $\nabla \times \mathbf{H} = 0$. Thus the magnetic field can then be written as the gradient of a scalar potential $\mathbf{H} = \nabla \psi_H$. This scalar potential then satisfies a scalar Laplace equation,

$$\partial_i \mu_{ij}(\omega) \partial_j \psi_H = 0, \tag{2}$$

where we have used repeated indices to denote summation. In this paper, the absence of applied magnetic fields guarantees that μ_{ij} is diagonal, and so Eq. (2) contains only three terms. Applying boundary conditions for the continuity of $\mathbf{B}$ in the z direction and of $\mathbf{H}$ in the xy plane at the two interfaces of a film of thickness d gives the dispersion relation

$$q_n = \frac{1}{2d\sqrt{-\mu(\omega)}}\left[\tan^{-1}\left(\frac{1}{\sqrt{-\mu(\omega)}}\right) + \frac{n\pi}{2}\right], \tag{3}$$

where n is an integer, q_n is the in-plane wave vector of mode n, and $\mu(\omega)$ is the permeability given in Eq. (1). We see that q_n is inversely proportional to the thickness of the slab d, which is anticipated, as the thickness of the material sets the scale of the wave solution in the z direction. Identical to confined modes on thin films of plasmonic materials (silver and gold for instance), a thinner film results in a smaller wavelength. An extreme limiting case in plasmonics is graphene, in which an atomically thin layer is capable of confining surface plasmons with confinement factors of 200 [5]. Figure 2(c) shows plots of the scalar potential ψ_H associated with SMP modes on MnF_2, which is proportional to the magnetic field in direction of propagation. The scalar potential solutions to the Laplace equation take the form

$$\psi_H^n(\mathbf{r}, \omega) = \begin{cases} e^{i\mathbf{q}_n \cdot \rho} e^{-q_n |z|} & |z| > d/2 \\ \left(\frac{e^{-q_n d}}{f(q_n d)}\right) e^{i\mathbf{q}_n \cdot \rho} f(q_n z) & |z| < d/2, \end{cases} \tag{4}$$

where $\rho = (x, y)$ is the in-plane position, $f(x) = \cos(x)$ for even modes, and $f(x) = \sin(x)$ for odd modes. Taking the gradient of the scalar potential gives the fully vectorial magnetic field, which reveals that the SMP mode propagates in the in-plane direction $\hat{q}$ with circular polarization $\hat{\varepsilon}_{\mathbf{q}} = (\hat{q} + i\hat{z})/\sqrt{2}$. This polarization is well known to be typical of quasistatic surface polariton modes, whether they are the transverse magnetic modes associated with quasielectrostatic excitations or transverse electric modes associated with quasimagnetostatic excitations.

We now discuss the key properties of these surface modes, including their dispersion, confinement, velocities, and quality factor resulting from material losses. In Fig. 2(b), we plot the material-thickness-invariant dispersion relation $\omega(qd)$. The dimensionless wave vector qd indicates how the size of the in-plane wave vector compares to the thickness of the film. We note that we have incorporated the effect of loss into the dispersion by finding solutions with real frequency and complex wave vector. Our dispersion plots show the real part of the wave vector. In the lossless limit, the dispersion

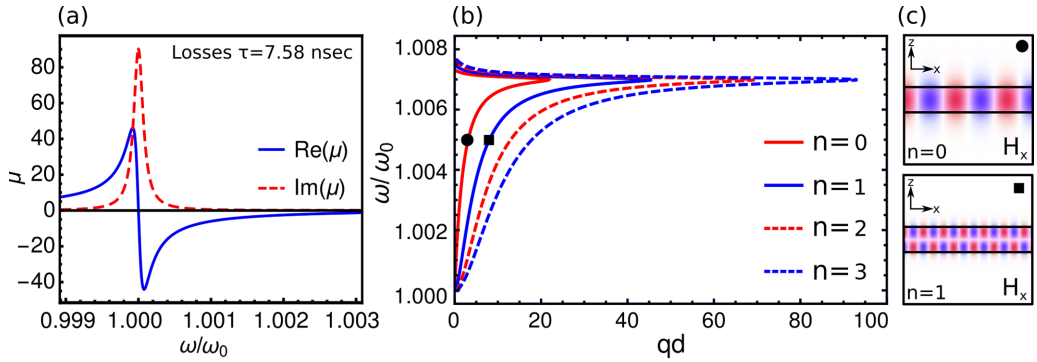

FIG. 2. Surface magnon polariton (SMP) modes on MnF_2. (a) Frequency-dependent permeability function for MnF_2 calculated using Eq. (1) and using the parameters given in Table I. For MnF_2, the resonance frequency is $\omega_0 = 1.68 \times 10^{12}$ rad/s. For $\omega_0 < \omega < \omega_{\max}$, $\mathrm{Re}(\mu) < 0$, allowing for surface modes. (b) Dispersion relation for MnF_2 of thickness d, calculated in the quasimagnetostatic limit which is valid in the range of thicknesses d we consider. The first four modes are shown. (c) Visualization of fundamental and first harmonic mode SMP through the field component H_x shown for a $d = 200$-nm film of MnF_2 at $\omega/\omega_0 = 1.005$. The locations of these two modes are indicated on the dispersion curve.

is asymptotic to a fixed frequency in the limit that $q \to \infty$. The introduction of loss causes the band to fold back on itself, placing a limit on the wave vectors which can be excited. Consequently, modes near the peak of this folded band exhibit the highest attenuation.

The dispersion plot shows the first four bands—the fundamental mode ($n = 0$) as well as three higher harmonics ($n = 1, 2, 3$). Due to the the reflection symmetry of the geometry in the z direction, two of these modes are even parity, and two are odd parity. We can interpret the mode index as the number of half oscillations which the magnetic field makes in the z direction of the film. Higher order modes will have larger wave vectors. Once again, we can further understand the dispersion relation of these modes through analogy to existing polaritonic systems. Specifically, MnF_2 is a hyperbolic material since $\mu_\perp > 0$ while $\mu_\parallel < 0$ (where the directions $\perp$ and $\parallel$ are taken with respect to the z axis). This is much like the naturally occurring hyperbolic material hexagonal boron nitride, which has one component of its permittivity negative, while another component is positive [18,19]. As a result of this, these systems have a multiply branched dispersion, and the electromagnetic fields are guided inside the crystal. The first two modes ($n = 0, 1$) are shown in Fig. 2(c), where we note the mode confinement to the slab, as well as the evanescent tails which enable interaction with surrounding emitters.

The most impressive figure of merit of these modes is the size of their wavelength in comparison to the free space wavelength at a given frequency, also known as a confinement factor or effective index of the mode. Figure 3(b) highlights this, showing the confinement factor $\eta = qc/\omega = \lambda_0/\lambda_{\mathrm{SMP}}$ for the first four modes ($n = 0, 1, 2, 3$) on $d = 200$ nm MnF_2 as a function of frequency. We see that the fundamental mode reaches a peak confinement of $\eta = 2 \times 10^4$, while the first harmonic is confined to twice that with $\eta = 4 \times 10^4$.

These values exceed by two orders of magnitude the maximum confinement values that have been observed in common plasmonic media such as thin films of silver, gold, or titanium nitride, or doped graphene. Furthermore, since the confinement scales linearly with $q \sim 1/d$, decreasing the material thickness increases the achievable range of confinement factors. As a simple example of this, consider that a material thickness of $d = 50$ nm would correspond to a wave vector four times larger than for $d = 200$ nm, in other words a maximum fundamental mode confinement of 8×10^4, and a confinement above 10^4 for much of the surface magnon band.

An explanation for this high confinement in terms of most basic principles is that the frequencies at which SMPs exist

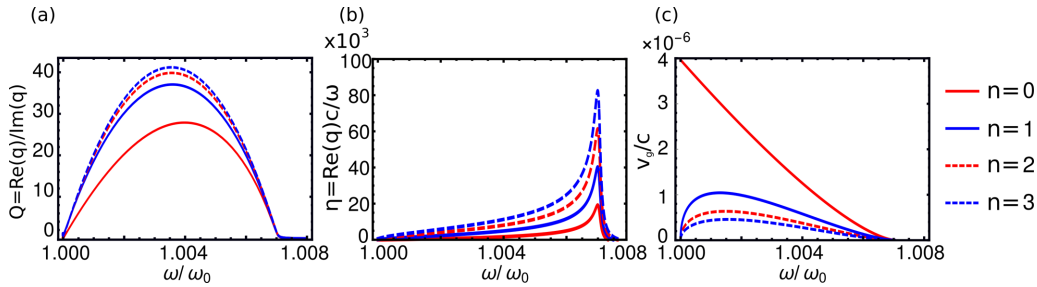

FIG. 3. Propagation properties of SMP modes on MnF_2. The following dimensionless quantities are plotted for MnF_2 with propagation loss $\tau = 7.58$ nsec for the first four modes indexed by $n = (0, 1, 2, 3)$: (a) mode quality factor $Q = \mathrm{Re}(q)/\mathrm{Im}(q)$ as a function of mode frequency, (b) mode confinement factor $\eta = qc/\omega$ as a function of mode frequency, and (c) normalized group velocity $v_g/c = |d\omega/dk|/c$ as a function of mode frequency.

(GHz-THz) are orders of magnitude lower than for plasmons which typically exist in IR to optical regimes. Simultaneously, the scale of the wave vector q in both plasmonic and magnonic media is set by the film thickness d for electrostatic and magnetostatic modes, respectively (this means that plasmons and magnons will have wave vectors of similar scale, regardless of frequency). In other words, at a fixed material thickness, lower frequency surface magnons have substantially higher potential for geometrical squeezing than surface plasmons. We note that this is not of purely formal interest, as when considering the enhancement of spontaneous emission, one finds that the enhancement is proportional to a power of precisely this confinement factor.

In addition to understanding the confinement of magnon polaritons, it is also important to understand their propagation characteristics, such as propagation quality factor, and group velocity. Figures 3(a) and 3(c) shows the quality factor $Q = \mathrm{Re}(q)/\mathrm{Im}(q)$, as well as the normalized group velocity v_g/c as a function of frequency for the first four modes. We see that propagation losses are lowest toward the middle of the allowed frequency band, showing quality factors greater than 20 for the fundamental mode ($n = 0$). Additionally, we see that the group velocity v_g reaches its maximum near the lower portion of the allowed frequency range, and goes toward zero at the other end.

II. THEORY OF SPIN RELAXATION INTO MAGNON POLARITONS

We now discuss how an an emitter with a magnetic dipole transition placed above the surface of a thin negative permeability material can undergo spontaneous emission into SMPs which is much faster than the emission into free space photons. First, we consider the Hamiltonian which couples the magnetic moment of the emitter to the quantized magnetic field. Fluctuations in the evanescent magnetic field from SMPs can then cause the emitter to relax via the emission of a SMP. The rate at which this process occurs is calculated using Fermi's golden rule. Finally, we discuss the effect of material losses on the total decay rate, and argue that for parameters of interest, the effect should be small.

We first discuss the mechanisms that can allow an emitter to couple to highly confined SMPs. A magnetic field can couple to both the electron spin angular momentum and orbital angular momentum, as both angular momenta contribute to the electron's magnetic moment. We describe this interaction quantum mechanically with an interaction Hamiltonian H_{int} between an emitter and a magnetic field [76,77]

$$H_{\mathrm{int}} = -\boldsymbol{\mu}\cdot\mathbf{B} = -\frac{\mu_B(\mathbf{L}+g\mathbf{S})}{\hbar}\cdot\mathbf{B}, \tag{5}$$

where $\boldsymbol{\mu}$ is the total magnetic moment of the emitter, $\mathbf{S} = \frac{\hbar}{2}\boldsymbol{\sigma}$ is the spin angular momentum operator, $\mathbf{L}$ is the orbital angular momentum operator, $g \approx 2.002$ is the Landé g-factor. In this Hamiltonian, we note that $\mathbf{B}$ is the quantized magnetic field operator associated with SMP modes.

To provide a fully quantum mechanical description of the interactions, we use the formalism of macroscopic QED (MQED) to rigorously quantize the electromagnetic field modes in a medium (in this case, a thin slab of negative permeability material) This approach is similar to that in Ref. [78], which was applied to quantize electromagnetic fields in dielectric structures. We consider a geometry of a negative μ material which is translation invariant (i.e., a slab geometry). In this case, the modes are labeled by an in-plane wave vector $\mathbf{q}$. We can then construct an operator which creates and annihilates excitations of the magnetic field which are normalized so each SMP carries energy $\hbar\omega_{\mathbf{q}}$. The magnetic field operator in the evanescent region above the slab ($z > d/2$) takes the form

$$\mathbf{B}(\mathbf{r}) = \sum_{\mathbf{q}}\sqrt{\frac{\mu_0\hbar\omega}{2AC_q}}(\hat{\varepsilon}_{\mathbf{q}}e^{i\mathbf{q}\cdot\rho}e^{-qz}a_{\mathbf{q}} + \hat{\varepsilon}^{*}_{\mathbf{q}}e^{-i\mathbf{q}\cdot\rho}e^{-qz}a^{\dagger}_{\mathbf{q}}), \tag{6}$$

where $a^{\dagger}_{\mathbf{q}}$ and $a_{\mathbf{q}}$ are creation and annihilation operators for the SMP modes satisfying the canonical commutation relation $[a_{\mathbf{q}}, a^{\dagger}_{\mathbf{q}'}] = \delta_{\mathbf{q}\mathbf{q}'}$, $\hat{\varepsilon}_{\mathbf{q}}$ is the mode polarization, A is the area normalization factor, and $C_q = \int dz\,\mathbf{H}^{*}(z)\cdot\frac{d(\mu\omega)}{d\omega}\cdot\mathbf{H}(z)$ is a normalization factor ensuring that the mode $\mathbf{H} = \boldsymbol{\nabla}\psi_H$ has an energy of $\hbar\omega_{\mathbf{q}}$. The energy has been calculated according to the Brillouin formula for the electromagnetic field energy in a dispersive medium in a transparency window [79,80]. As a point of comparison, we note that similar quantization schemes have been implemented for surface plasmon-polariton modes on graphene [22] and many other systems in optics [78,81]. In this expression for the energy, we have also used the fact that the modes are magnetostatic in nature, so the contribution of the electric field to the energy associated with them is negligible.

To establish the strength of the coupling between a magnetic dipole emitter and SMPs, we calculate spontaneous emission of a spin into a thin negative μ material such as an antiferromagnet, using Fermi's golden rule. The rate of transition via the emission of a magnon of wave vector $\mathbf{q}$ is given as

$$\Gamma^{(\mathrm{eg})}_{\mathbf{q}} = \frac{2\pi}{\hbar^2}|\langle \mathrm{g}, \mathbf{q}|H_{\mathrm{int}}|\mathrm{e}, 0\rangle|^2\delta(\omega_{\mathbf{q}} - \omega_{\mathrm{eg}}). \tag{7}$$

We specify the initial and final states of the system as $|\mathrm{e}, 0\rangle$ and $|\mathrm{g}, \mathbf{q}\rangle$, respectively, where e and g index the excited and ground states of the emitter, $\mathbf{q}$ is the wave vector of the magnon resulting from spontaneous emission, $\omega_{\mathbf{q}}$ is its corresponding frequency, and ω_{eg} is the frequency of the spin transition. Note that Eq. (7) applies generally and can capture any multipolar magnetic transition.

With the magnetic field quantized appropriately and the interaction Hamiltonian established, obtaining the spontaneous emission rate proceeds in the usual way. Substituting Eq. (6) into the Hamiltonian of Eq. (5), and then applying Fermi's golden rule as written in Eq. (7), we find that the spontaneous emission rate $\Gamma^{(\mathrm{eg})}$ per unit magnon in-plane propagation angle θ is given by

$$\frac{d\Gamma^{(\mathrm{eg})}_{\mathrm{dipole}}}{d\theta} = \frac{\mu_B^2\mu_0\omega_{\mathrm{eg}}}{2\pi\hbar}\frac{q^3(\omega_{\mathrm{eg}})}{C_q(\omega_{\mathrm{eg}})|v_g(\omega_{\mathrm{eg}})|}e^{-2q(\omega_{\mathrm{eg}})z_0}|M_{\mathrm{eg}}|^2, \tag{8}$$

where $|v_g| = |\boldsymbol{\nabla}_{\mathbf{q}}\omega|$ is the magnitude of the SMP group velocity, μ_B is the Bohr magneton, and $M_{eg} = \langle g|\hat{\epsilon}_{\mathbf{q}}\cdot(\mathbf{L}+g\mathbf{S})|e\rangle$ is the matrix element which describes the transition. Also note that here we have made the dipole approximation for magnetic

transitions, which comes from assuming that the evanescent field of the emitted SMP varies negligibly over the size of the emitter, and can thus be assumed constant. However, if one wishes to remove this simplifying assumption to consider magnetic multipole transitions, the matrix element can be numerically evaluated. To simplify the proceeding discussion, we focus on cases where the transition corresponds only to a change of spin of the electron in the emitter from $|\uparrow\rangle$ to $|\downarrow\rangle$, this matrix element is simply proportional to $\boldsymbol{\sigma}_{\rm eg} = \langle\downarrow|\boldsymbol{\sigma}\cdot\hat{\boldsymbol{\varepsilon}}_{\mathbf{q}}|\uparrow\rangle$. Here, the angular dependence can come solely from the magnon polarization. For a spin transition oriented along the z (i.e., out-of-plane) axis, the transition strength into modes at different θ will be the same, and thus the distribution of emitted magnons isotropic. Spin transitions along a different axis will break this symmetry, resulting in angle-dependent emission. In any case, the total rate of emission is obtained by integrating over all angles as $\Gamma^{(\rm eg)}_{\rm dipole} = \int_0^{2\pi}\left(\frac{d\Gamma^{(\rm eg)}}{d\theta}\right)d\theta$.

We now consider the effect of material losses, and argue that the lossless approximation for decay rates presented here should provide a strong approximation for decay rates in the presence of losses. The formalism of macroscopic QED detailed in Ref. [34] can be used to incorporate material losses into spontaneous emission calculations. It was found explicitly in Ref. [14] that, in general, the presence of losses does not drastically change the total decay rate of the emitter, unless the emitter is at distances from the material much smaller than the inverse wave vector of the modes that are emitted. For the case of relatively low losses, Fermi's golden rule shown in Eq. (7) can be modified by replacing the delta function density of states with a Lorentzian of width $\Delta\omega \equiv 1/\tau$. The lossy decay rate is then obtained as a convolution of this Lorentzian frequency spread with the lossless rate as

$$\Gamma^{(\rm eg)}_{\rm dipole} \longrightarrow \int \Gamma^{(\rm eg)}_{\rm dipole}\left(\frac{1}{\pi}\frac{1/(2\tau)}{(\omega_{\rm eg}-\omega)^2+(1/2\tau)^2}\right)d\omega. \quad (9)$$

In general, this correction from losses will be small provided that the range of frequencies $\Delta\omega$ coupled by Eq. (9) is small compared to the width of the magnon band, denoted $\Delta\Omega$. More succinctly, losses are negligible if $\Delta\omega/\Delta\Omega \ll 1$. For the MnF_2 considered here, $\Delta\omega \approx 10^{-8}$ s^{-1}, and $\Delta\Omega \approx 10^{10}$ s^{-1}, so $\Delta\omega/\Delta\Omega \approx 10^{-2}$, confirming that the Lorentzian distribution behaves similarly to a delta function $\delta(\omega_{\rm eg}-\omega)$ which does not mix frequencies. Having presented the general framework for analyzing SMP emission, we now present specific results for SMP emission into a thin film of MnF_2.

III. TRANSITION RATE RESULTS

A. Dipole transition rates

We first discuss the transition rates and associated Purcell factors of magnetic dipole emitters. For a z-oriented spin flip of frequency $\omega_{\rm eg}$ placed a distance z_0 from the surface of a negative μ film, the spontaneous emission rate is given as

$$\Gamma^{(\rm eg)}_{\rm dipole} = \frac{\mu_B^2\mu_0\omega_{\rm eg}}{\hbar}\frac{q^2(\omega_{\rm eg})}{C'(\omega_{\rm eg})|v_g(\omega_{\rm eg})|}e^{-2q(\omega_{\rm eg})z_0}, \quad (10)$$

where $C'(\omega) = C(\omega)/q(\omega)$ is introduced to remove the wave-vector dependence from the normalization. We also note that the group velocity $|v_g(\omega)| \propto 1/q(\omega)$, and thus the whole expression, carries a wave-vector dependence of $\Gamma^{(\rm eg)}_{\rm dipole} \propto q^3(\omega_{\rm eg})$.

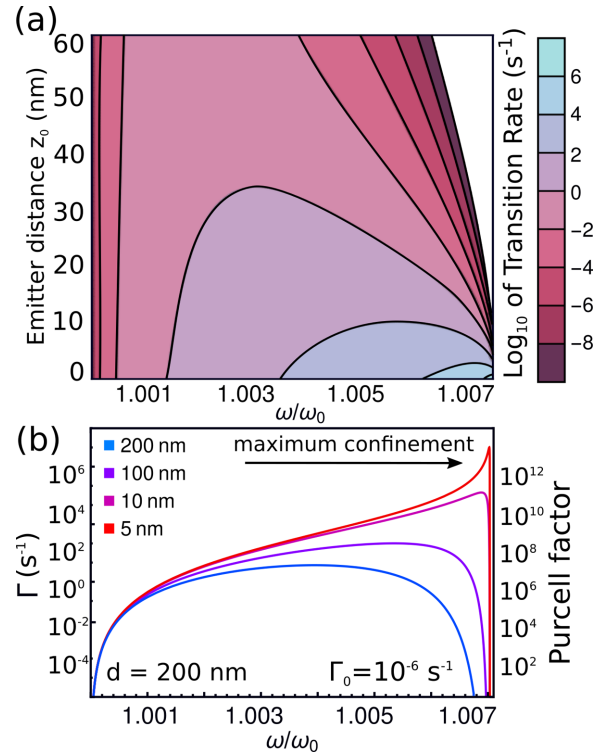

FIG. 4. Dipole transition rate enhancement by SMPs. (a) Dipole transition rate for a z-oriented spin flip as a function of normalized frequency and distance z_0 from the emitter to the surface of a $d = 200$ nm MnF_2 film. The transition rates decay exponentially with increasing distance from the surface. (b) Line cuts of the information shown in (a) for different fixed distances z_0. The axis on the left shows the total transition rate, while the axis on the right shows the Purcell factor; in other words, the transition rate normalized by the free space transition rate.

We now discuss the numerical values for spin-flip transition rates in nearby emitters which come directly from Eq. (10). We find these transition rates into SMPs to be orders of magnitude faster than the rates of transition into free-space photons at the same frequency. Figure 4 shows the emission rate as a function of frequency ω and emitter distance z_0 for a $d = 200$ nm MnF_2 film. Figure 4(b) shows line cuts of the dipole transition rate at various emitter distances z_0. In this geometry, we find that for the highest supported magnon frequencies, the total rate of emission may exceed 10^5 s^{-1}, which corresponds to a decay time of 10 μs. This is 11 orders of magnitude of improvement over the free-space decay lifetime of more than a week. We see that for sufficiently close distances z_0, the decay rate increases with ω, spanning many orders of magnitude over a small frequency bandwidth. Furthermore, we see that with increasing distance z_0, the total decay rate is suppressed exponentially by the evanescent tail of the surface magnon. More specifically, we see in the exponential dependence $e^{-2q(\omega_{\rm eg})z_0}$ that, for rate enhancement to be effective, z_0 should be comparable to or ideally smaller than $1/q \sim d$. For a 200-nm film, enhancement begins to

saturate for $z_0 < 20$ nm. In terms of a potential experiment, these are promising parameters which could result in a total transition rate of 10^4 s^{-1}. Finally, we note that at distances z_0 extremely near to the surface, effects such as material losses or nonlocality may cause the behavior of the transition rate to deviate slightly from the predicted behavior. The exact magnitude of such effects could be taken into account directly by solving for the dispersion with the full, nonlocal, magnetic susceptibility which is presented in Ref. [68].

It is also worthwhile to consider not only the total transition rates, but also the Purcell factors. The right side axis of Fig. 4(b) shows the Purcell factor for spin relaxation into SMPs, computed as the ratio between the enhanced transition rate and the free-space transition rate, and denoted as $F_p(\omega) = \Gamma_{\text{dipole}}/\Gamma_0$. We note that while the transition rate in the magnonic environment is technically the sum of the SMP emission rate and the radiative rate, in our systems the radiative rate is so small that it need not be considered.

Thinner films offer even more drastic capabilities for enhancement. The dipole transition rate and Purcell factor scale as η^3, which means that shrinking the film thickness d even by conservative factors can result in a rapid increase in the maximum transition rate achievable. This η^3 scaling is exactly the same scaling found for Purcell factors of electric dipole transition enhancement in the vicinity of highly confined electrostatic modes such as surface plasmon polaritons [14,17,33].

Having established the duality between electric and magnetic surface polaritonics in the context of Purcell enhancement, other important conclusions about the scope and utility of SMPs follow. Most notably, Purcell factors for higher order magnetic processes should scale with mode confinement identical to those for the corresponding electric processes. Given an emitter-material system that can support such processes, it should be possible to compute transition rates of higher order processes such as magnetic quadrupole transitions and multimagnon emission processes. Conveniently, electromagnetic duality implies that the confinement scaling properties of all electric multipolar or multiphoton transitions into electric polaritons are identical to those of their magnetic analogs. For example, the magnetic quadrupole transition Purcell factor should scale as $\propto \eta^5$. For emission into modes confined to factors of 1000 or more, this enhancement factor could easily exceed 10^{15}, alluding to the possibility of making highly forbidden magnetic quadrupole processes observable.

B. Emission with in-plane anisotropy

Thus far, we have considered geometries of MnF_2 in which the anisotropy axis of the crystal is out of the plane of a thin film (in the z direction). Past work has brought both theoretical interest as well as experimental studies on antiferromagnetic surface interfaces in which the magnetic permeability anisotropy axis lies in plane. In other words, the material has negative permeability in the out-of-plane direction as well as one in-plane direction, while having a permeability of 1 in the other in-plane direction. This geometry gives rise to an rich anisotropic dispersion relation of SMP modes, which in turn result in a nontrivial angular dependence for processes of spontaneous emission. We summarize those findings here.

For the in-plane anisotropic geometry with $\mu = (\mu(\omega), 1, \mu(\omega))$, the dispersion (obtained again by solving Maxwell's equations for a quasimagnetostatic scalar potential) is given by solutions to

$$e^{qd\sqrt{\beta(\theta,\omega)}} = \frac{1-\mu(\omega)\sqrt{\beta(\theta,\omega)}}{1+\mu(\omega)\sqrt{\beta(\theta,\omega)}}, \tag{11}$$

where $\beta(\theta,\omega) = \cos^2\theta + \sin^2\theta/\mu(\omega)$ and θ is the in-plane propagation angle measured with respect to the x axis. When $\beta > 0$, the mode function has a z dependence of $\cosh(qz)$ or $\sinh(qz)$, dependent on the parity of the solution. When $\beta < 0$, the modes have a $\cos(qz)$ or $\sin(qz)$ dependence. We note that the $\beta < 0$ solutions have a multiply branched structure which correspond to higher harmonic modes, just as with the in-plane isotropic case discussed throughout the text. Furthermore, recalling that $\mu < 0$ and examining $\beta(\theta,\omega)$, we see that for angles of propagation near 0, β will be positive, while for angles of propagation near $\pi/2$, β is negative. Based on the sign of β, we can classify the modes into two distinct types. We refer to $\beta > 0$ modes as type-I modes and $\beta < 0$ modes as type-II modes. The fundamental type-I modes propagate in the range $\theta \in (0, \theta_x)$, where $\theta_x = \tan^{-1}(\sqrt{-\mu(\omega)})$, while the type-II modes with $n = 1$ propagate in the range $\theta \in (\theta_y, \pi/2)$, with $\theta_y = \cos^{-1}(1/\sqrt{-\mu(\omega)})$. The angular propagation ranges for the type-I modes and the lowest order type-II mode are nonoverlapping and the gap between θ_x and θ_y increases with ω.

The dispersion for even type-I and type-II modes are, respectively, given as

$$q_{\text{I}} = -\frac{1}{2d\sqrt{\beta(\theta,\omega)}}\tanh^{-1}\left(\frac{1}{\mu(\omega)\sqrt{\beta(\theta,\omega)}}\right), \tag{12}$$

$$q^n_{\text{II}} = \frac{1}{2d\sqrt{-\beta(\theta,\omega)}}\tan^{-1}\left(\frac{1}{\mu(\omega)\sqrt{-\beta(\theta,\omega)}} + \frac{n\pi}{2}\right), \tag{13}$$

where n is an integer. We see that for even type-I modes, only a single band of surface polariton modes exists, while for type-II modes, a richer structure with harmonics exists due to the multivalued nature of the arctangent, just as in the in-plane isotropic case. In Fig. 5, we see the isofrequency contours for the dispersion in the case of in-plane anisotropy. We clearly observe that the mode structure is anisotropic, in that type-I modes behave differently than type-II modes. We comment briefly on the polarization of the modes. The in-slab **H**-field polarization of the type-I and -II modes are, respectively, given as

$$\hat{\varepsilon}_q = \begin{cases} \frac{\hat{q}\cosh(qz)+i\sinh(qz)\hat{z}}{\sqrt{2}}, & \text{type I} \\ \frac{\hat{q}\cos(qz)+i\sin(qz)\hat{z}}{\sqrt{2}}, & \text{type II.} \end{cases} \tag{14}$$

Applying the same formalism as before, the rate of emission into SMPs per unit angle by a z-oriented spin flip of strength μ_B is given by

$$\frac{d\Gamma^{(\text{eg})}}{d\theta} = \frac{\mu_B^2\mu_0\omega_{\text{eg}}}{2\pi\hbar}\frac{q^3(\theta,\omega_{\text{eg}})|\boldsymbol{\sigma}_{eg}\cdot\hat{\boldsymbol{\epsilon}}_{\mathbf{q}}|^2}{C_q(\theta,\omega_{\text{eg}})|v_g(\theta,\omega_{\text{eg}})|}e^{-2q(\theta,\omega_{\text{eg}})z_0}. \tag{15}$$

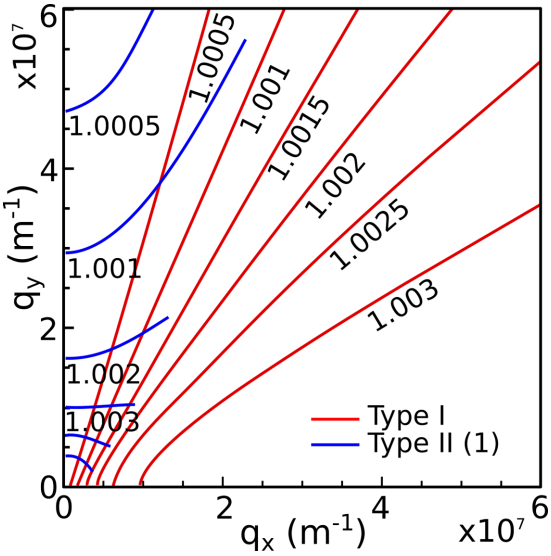

FIG. 5. Dispersion for anisotropic modes. Isofrequency contours for MnF_2 of thickness $d = 200$ nm. The frequency labels are given as ω/ω_0, where ω_0 is the resonance frequency of the material. The first type-I modes are shown in red, while the type-II modes with $n = 1$ are shown in blue.

The total rate is obtained by integrating over all angles:

$$\Gamma^{(\mathrm{eg})} = \frac{\mu_B^2 \mu_0 \omega_{\mathrm{eg}}}{2\pi\hbar} \int_0^{2\pi} \frac{q^3(\theta, \omega_{\mathrm{eg}}) |\boldsymbol{\sigma}_{eg} \cdot \hat{\epsilon}_{\mathbf{q}}|^2}{C_q(\theta, \omega_{\mathrm{eg}}) |v_g(\theta, \omega_{\mathrm{eg}})|} e^{-2q(\theta,\omega_{\mathrm{eg}})z_0} d\theta. \tag{16}$$

In Fig. 6 we see the lossless differential decay rate $d\Gamma^{(eg)}/d\theta$ plotted as a function of polar angle θ for a z-oriented spin-flip transition at different emitter frequencies ω. We see that with increasing frequency, the angular spread of type-I modes narrows, while the angular spread of type-II modes increases. We can understand this behavior in terms of the availability and confinement of modes for different propagation angles θ. The most highly confined modes are the type-I modes near the angular cutoff. As ω increases the confinement of type-I modes at low angles increases, while the confinement of type-II modes decreases. This system exhibits the interesting property that tuning the frequency of the emitter over a narrow bandwidth dramatically shapes the angular spectrum of polariton emission. An interesting consequence is that for an emitter with a broadened spectral line (broader than $0.001\omega_0$), the angular spectrum will be a complicated mixture of the qualitatively different angular spectra in Fig. 6.

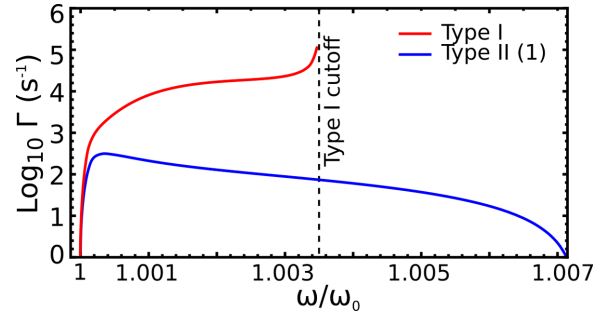

FIG. 7. Magnetic dipole transition rate for in-plane anisotropic MnF_2. Magnetic dipole transition rate for a z-oriented dipole transition a distance $z_0 = 5$ nm from the surface into two different SMP modes in a $d = 200$-nm-thick anisotropic slab of MnF_2. The type-I mode emits most strongly but over a narrower range of frequencies. The cutoff frequency is the frequency at which the first type I mode no longer satisfies the boundary conditions. The first-order type-II mode is emitted more weakly but is supported over the entire range of frequencies for which $\mu(\omega) < 0$.

In Fig. 7, we see the total transition rate $\Gamma^{(eg)}$ for a dipole emitter above MnF_2 oriented with the anisotropy axis in the y direction. While the transition rates of both modes are greatly enhanced compared to the free-space transition rate of order $10^{-6}\ s^{-1}$, the type-I mode benefits approximately two orders of magnitude more than the first type-II mode. In particular, the Purcell factor for the type-I mode ranges from 10^{10} to 10^{12}, and is thus quite comparable to Purcell factors obtained for the in-plane isotropic discussed previously. In this sense, we see that extreme enhancement of magnetic dipole transition

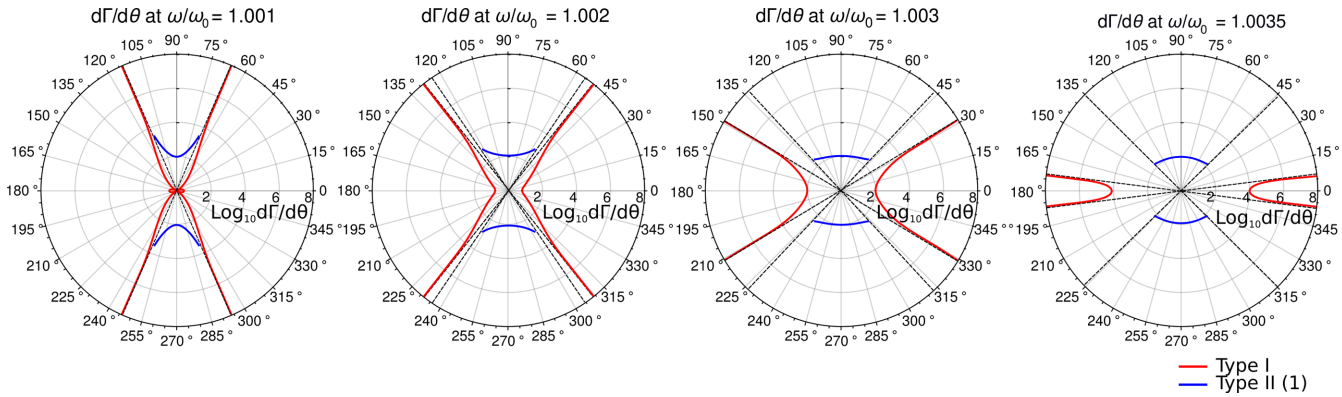

FIG. 6. Angular distribution of SMP emission. Magnetic dipole transition rate per unit angle $d\Gamma^{(eg)}/d\theta$ for radiation into SMPs on a 200-nm-thick slab of MnF_2. The radial axis shows $d\Gamma^{(eg)}/d\theta$ plotted on a log scale in units of s^{-1}. The first type-I modes are shown in red and the first type-II modes are shown in blue. Dashed lines indicate the angular cutoffs θ_x and θ_y for each type of mode. Note that at low frequencies, θ_x and θ_y become very close. We additionally note that for $\omega/\omega_0 > 1.0035$, the type-I mode branch shown in red vanishes entirely, leaving only the type-II modes.

rates is achievable in both crystal orientations. The dispersion relation, however, is notably different in these cases. As an additional degree of freedom, one can consider how the dispersion, and consequently the dipole emission rate, will be influenced by an applied magnetic field along the anisotropy axis of a material such as MnF_2. In this case, an effective Zeeman splitting causes the resonance frequency ω_0 to split into two frequencies which move away from each other in linear proportion to the applied field, as described, for example, in Ref. [82]. When the anisotropy axis lies in the plane of the material, such an applied field results in nonreciprocal propagation of waves due to the broken reflection symmetry. For these reasons, applied fields may be used to tune the AFMR frequencies or to shape the properties of the spin waves emitted by magnetic dipole transitions. The net result is a highly flexible platform for strong interaction between magnetic transitions and matter.

IV. EXPERIMENTAL CONSIDERATIONS AND OUTLOOK

We have shown that highly confined SMPs, such as those on antiferromagnetic materials, could speed up magnetic transitions by more than ten orders of magnitude, bridging the inherent gap in decay rates which typically separates electric and magnetic processes. We predict that these confined magnetic surface modes in systems with realizable parameters may exhibit confinement factors in excess of 10^4. We developed the theory of magnon polaritons and their interactions with emitters in a way that unifies this set of materials with other more well-known polaritonic materials, casting light on opportunities to use these materials to gain unprecedented control over spins in emitters.

To push the field of magnon polaritonics at THz frequencies forward, it will be necessary to identify an ideal experimental platform for manipulating these modes and interfacing them with matter. For antiferromagnetic platforms, experiments will need to take place below the Néel temperature of the material to establish antiferromagnetic order. Importantly, we note that the only strict material requirement for SMPs is that $\mathrm{Re}(\mu) < 0$ over some frequency range, presenting opportunities for other types of magnetic order, 2D magnetic materials, or even metamaterials which exhibit negative permeability. The other key consideration is what class of emitters may be well-suited to interact with these polaritonic modes. In terms of existing materials, a potential emitter system which can interact with the antiferromagnetic SMPs discussed here is $ErFeO_3$, which has several electric and magnetic dipole transitions in the range between 0.25 and 1.5 THz [83]. Recent work has also considered THz magnon polaritons in $TmFeO_3$ [84]. It could also prove interesting to consider GHz-THz orbital angular momentum transitions between high-energy levels in Rydberg atoms, Landau levels, or vibrational modes in molecules. In addition, one could consider THz transitions arising from impurity states in semiconductors [85], which have the benefit of the tunability over THz scale by the application of an external magnetic field.

The theoretical predictions made in this paper could be verified by fluorescence spectroscopy measurements on a thin layered sample as shown in Fig. 8. We represent the emitter as a three-level system, where the gap between the lower level and the higher levels is in the optical/IR and is excited with an external laser via an electric dipole transition. The excited state can then decay into SMPs in the material below via a magnetic dipole transition. Such a magnetic dipole transition is usually very slow in free space, but as detailed in our paper, will occur orders of magnitude faster due to decay into SMPs. The emitter state populations and transition rates can then be monitored via spectroscopy of the optical photon emitted to free space. One would expect to see a decrease in fluorescence at the exciting laser frequency, in conjunction with the appearance of a new Raman peak, shifted from the exciting frequency by the THz SMP frequency. Similar schemes for monitoring Purcell enhancements in plasmonics have been implemented in Ref. [86]. Time-resolved measurements have also been made in Ref. [87] to directly measure the decay in excited state populations which occurs through Purcell-enhanced emission of polaritons. Alternatively, a substantial rate increase in a THz MD transition due to SMP excitation could influence rate dynamics in a way which produces optical/IR far-field decays at frequencies entirely different from the exciting laser. Methods for analyzing such mechanisms are detailed in Ref. [88].

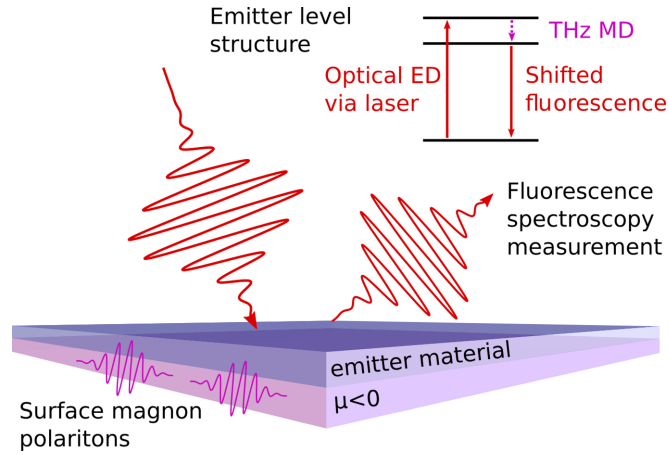

FIG. 8. Schematic for a potential fluorescence spectroscopy experiment to observe enhancement of magnetic dipole (MD) transitions through surface magnon polaritons. We consider a layered sample which contains a thin negative permeability film which supports SMPs and a material containing an appropriately chosen emitter material. An external laser prepares the emitters into an excited state via an IR/optical transition. This excited state then decays via a THz transition into SMPs in the thin film and then relaxes via a photon transition into the far field. The far-field signal can be measured with a spectrometer to detect the Raman shift in the fluorescence frequency compared to the incident laser frequency.

Future work could also consider processes involving the emission of multiple surface magnons using the framework presented in Ref. [33] or mixed processes with the emission of a magnon polariton in addition to one or more excitations of another nearby material. In any case, SMPs provide an interesting degree of control over magnetic degrees of freedom in matter as well as a means to consider magnetic analogs at THz frequencies of many famous effects in plasmonics and polaritonics.

ACKNOWLEDGMENTS

The authors thank C. Roques-Carmes and N. Romeo for help reviewing the paper. Research was supported as part of the Army Research Office through the Institute for Soldier Nanotechnologies under Contract No. W911NF-18-2-0048 (photon management for developing nuclear-TPV and fuel-TPV mm-scale systems), also supported as part of the S3TEC, an Energy Frontier Research Center funded by the US Department of Energy under Grant No. DE-SC0001299 (for fundamental photon transport related to solar TPVs and solar-TEs). I.K. acknowledges support as an A. Fellow, supported by the Azrieli Foundation, and was partially supported by the Seventh Framework Programme of the European Research Council (FP7-Marie Curie IOF) under Grant No. 328853-MC-BSiCS. N.R. recognizes the support of the DOE Computational Science Graduate Fellowship (CSGF) No. DE-FG02-97ER25308.

[1] H. A. Atwater, Sci. Am. **296**, 56 (2007).
[2] D. N. Basov, M. M. Fogler, and F. J. García de Abajo, Science **354**, aag1992 (2016).
[3] D. Basov, R. Averitt, and D. Hsieh, Nat. Mater. **16**, 1077 (2017).
[4] T. Low, A. Chaves, J. D. Caldwell, A. Kumar, N. X. Fang, P. Avouris, T. F. Heinz, F. Guinea, L. Martin-Moreno, and F. Koppens, Nat. Mater. **16**, 182 (2017).
[5] D. A. Iranzo, S. Nanot, E. J. Dias, I. Epstein, C. Peng, D. K. Efetov, M. B. Lundeberg, R. Parret, J. Osmond, J.-Y. Hong *et al.*, Science **360**, 291 (2018).
[6] G. Ni, A. McLeod, Z. Sun, L. Wang, L. Xiong, K. Post, S. Sunku, B.-Y. Jiang, J. Hone, C. Dean *et al.*, Nature **557**, 530 (2018).
[7] M. Moskovits, Rev. Mod. Phys. **57**, 783 (1985).
[8] M. G. Albrecht and J. A. Creighton, J. Am. Chem. Soc. **99**, 5215 (1977).
[9] D. L. Jeanmaire and R. P. Van Duyne, J. Electroanal. Chem. Interfacial Electrochem. **84**, 1 (1977).
[10] S. Nie and S. R. Emory, Science **275**, 1102 (1997).
[11] M. Kauranen and A. V. Zayats, Nat. Photonics **6**, 737 (2012).
[12] M. L. Andersen, S. Stobbe, A. S. Sørensen, and P. Lodahl, Nat. Phys. **7**, 215 (2011).
[13] M. Takase, H. Ajiki, Y. Mizumoto, K. Komeda, M. Nara, H. Nabika, S. Yasuda, H. Ishihara, and K. Murakoshi, Nat. Photonics **7**, 550 (2013).
[14] N. Rivera, I. Kaminer, B. Zhen, J. D. Joannopoulos, and M. Soljačić, Science **353**, 263 (2016).
[15] F. Machado, N. Rivera, H. Buljan, M. Soljacic, and I. Kaminer, ACS Photon. **5**, 3064 (2018).
[16] Y. Kurman, N. Rivera, T. Christensen, S. Tsesses, M. Orenstein, M. Soljačić, J. D. Joannopoulos, and I. Kaminer, Nat. Photon. **12**, 423 (2018).
[17] J. D. Caldwell, O. J. Glembocki, Y. Francescato, N. Sharac, V. Giannini, F. J. Bezares, J. P. Long, J. C. Owrutsky, I. Vurgaftman, J. G. Tischler *et al.*, Nano Lett. **13**, 3690 (2013).
[18] J. D. Caldwell, A. V. Kretinin, Y. Chen, V. Giannini, M. M. Fogler, Y. Francescato, C. T. Ellis, J. G. Tischler, C. R. Woods, A. J. Giles *et al.*, Nat. Commun. **5**, 5221 (2014).
[19] S. Dai, Z. Fei, Q. Ma, A. Rodin, M. Wagner, A. McLeod, M. Liu, W. Gannett, W. Regan, K. Watanabe *et al.*, Science **343**, 1125 (2014).
[20] J. D. Caldwell, L. Lindsay, V. Giannini, I. Vurgaftman, T. L. Reinecke, S. A. Maier, and O. J. Glembocki, Nanophotonics **4**, 44 (2015).
[21] E. Purcell, Phys. Rev. **69**, 681 (1946).
[22] X. Lin, N. Rivera, J. J. López, I. Kaminer, H. Chen, and M. Soljačić, New J. Phys. **18**, 105007 (2016).
[23] J. B. Khurgin, Nanophotonics **7**, 305 (2018).
[24] J. B. Khurgin, Nat. Nanotech. **10**, 2 (2015).
[25] B. Rolly, B. Bebey, S. Bidault, B. Stout, and N. Bonod, Phys. Rev. B **85**, 245432 (2012).
[26] R. Hussain, S. S. Kruk, C. E. Bonner, M. A. Noginov, I. Staude, Y. S. Kivshar, N. Noginova, and D. N. Neshev, Opt. Lett. **40**, 1659 (2015).
[27] A. Slobozhanyuk, A. Poddubny, A. Krasnok, and P. Belov, Appl. Phys. Lett. **104**, 161105 (2014).
[28] A. M. Mahmoud and N. Engheta, Nat. Commun. **5**, 5638 (2014).
[29] D. G. Baranov, R. S. Savelev, S. V. Li, A. E. Krasnok, and A. Alù, Laser Photonics Rev. **11**, 1600268 (2017).
[30] F. H. Koppens, D. E. Chang, and F. J. Garcia de Abajo, Nano Lett. **11**, 3370 (2011).
[31] A. Kumar, T. Low, K. H. Fung, P. Avouris, and N. X. Fang, Nano Lett. **15**, 3172 (2015).
[32] O. D. Miller, O. Ilic, T. Christensen, M. H. Reid, H. A. Atwater, J. D. Joannopoulos, M. Soljačicć, and S. G. Johnson, Nano Lett. **17**, 5408 (2017).
[33] N. Rivera, G. Rosolen, J. D. Joannopoulos, I. Kaminer, and M. Soljačić, Proc. Natl. Acad. Sci. **114**, 13607 (2017).
[34] S. Scheel and S. Buhmann, Acta Physica Slovaca. Rev. Tutorials **58**, 675 (2008).
[35] S. Y. Buhmann and S. Scheel, Phys. Rev. Lett. **102**, 140404 (2009).
[36] D. Mills and E. Burstein, Rep. Prog. Phys. **37**, 817 (1974).
[37] M. I. Kaganov, N. Pustyl'nik, and T. Shalaeva, Phys. Usp. **40**, 181 (1997).
[38] R. Macêdo, in *Solid State Physics* (Elsevier, Cambridge, MA, 2017), Vol. 68, pp. 91–155.
[39] D. D. Stancil and A. Prabhakar, *Spin Waves* (Springer, New York, 2009).
[40] J. Des Cloizeaux and J. Pearson, Phys. Rev. **128**, 2131 (1962).
[41] P. W. Anderson, Phys. Rev. **86**, 694 (1952).
[42] T. Oguchi, Phys. Rev. **117**, 117 (1960).
[43] F. D. M. Haldane, Phys. Rev. Lett. **50**, 1153 (1983).
[44] M. Takahashi, Phys. Rev. B **40**, 2494 (1989).
[45] A. Auerbach and D. P. Arovas, Phys. Rev. Lett. **61**, 617 (1988).
[46] L. Berger, Phys. Rev. B **54**, 9353 (1996).
[47] C. Kittel, Phys. Rev. **110**, 1295 (1958).
[48] A. Chumak, V. Vasyuchka, A. Serga, and B. Hillebrands, Nat. Phys. **11**, 453 (2015).
[49] A. V. Chumak, A. A. Serga, and B. Hillebrands, Nat. Commun. **5**, 4700 (2014).
[50] T. Kampfrath, A. Sell, G. Klatt, A. Pashkin, S. Mährlein, T. Dekorsy, M. Wolf, M. Fiebig, A. Leitenstorfer, and R. Huber, Nat. Photon. **5**, 31 (2011).

[51] I. Žutić, J. Fabian, and S. D. Sarma, Rev. Mod. Phys. **76**, 323 (2004).

[52] S. Wolf, D. Awschalom, R. Buhrman, J. Daughton, S. Von Molnar, M. Roukes, A. Y. Chtchelkanova, and D. Treger, Science **294**, 1488 (2001).

[53] L. Bogani and W. Wernsdorfer, in *Nanoscience and Technology: A Collection of Reviews from Nature Journals* (World Scientific, Singapore, 2010), pp. 194–201.

[54] A. R. Rocha, V. M. Garcia-Suarez, S. W. Bailey, C. J. Lambert, J. Ferrer, and S. Sanvito, Nat. Mater. **4**, 335 (2005).

[55] V. Baltz, A. Manchon, M. Tsoi, T. Moriyama, T. Ono, and Y. Tserkovnyak, Rev. Mod. Phys. **90**, 015005 (2018).

[56] R. L. Stamps, S. Breitkreutz, J. Åkerman, A. V. Chumak, Y. Otani, G. E. Bauer, J.-U. Thiele, M. Bowen, S. A. Majetich, M. Kläui *et al.*, J. Phys. D **47**, 333001 (2014).

[57] A. Serga, A. Chumak, and B. Hillebrands, J. Phys. D **43**, 264002 (2010).

[58] N. S. Almeida and D. L. Mills, Phys. Rev. B **37**, 3400 (1988).

[59] R. E. Camley and D. L. Mills, Phys. Rev. B **26**, 1280 (1982).

[60] C. Shu and A. Caillé, Solid State Commun. **42**, 233 (1982).

[61] J. Eshbach and R. Damon, Phys. Rev. **118**, 1208 (1960).

[62] T. L. Gilbert, IEEE Transactions on Magnetics **40**, 3443 (2004).

[63] E. M. Lifshitz and L. P. Pitaevskii, *Statistical Physics: Theory of the Condensed State* (Elsevier, Oxford, 2013), Vol. 9.

[64] J. Stout and S. A. Reed, J. Am. Chem. Soc. **76**, 5279 (1954).

[65] C. Kittel, Phys. Rev. **82**, 565 (1951).

[66] B. Lüthi, D. L. Mills, and R. E. Camley, Phys. Rev. B **28**, 1475 (1983).

[67] R. Macêdo and T. Dumelow, Phys. Rev. B **89**, 035135 (2014).

[68] A. I. Akhiezer, S. Peletminskii, and V. G. Baryakhtar, *Spin Waves* (North-Holland, Amsterdam, 1968).

[69] T. Dumelow and M. C. Oliveros, Phys. Rev. B **55**, 994 (1997).

[70] L. Remer, B. Lüthi, H. Sauer, R. Geick, and R. E. Camley, Phys. Rev. Lett. **56**, 2752 (1986).

[71] R. Greene, D. Sell, W. Yen, A. Schawlow, and R. White, Phys. Rev. Lett. **15**, 656 (1965).

[72] R. L. Stamps, B. L. Johnson, and R. E. Camley, Phys. Rev. B **43**, 3626 (1991).

[73] M. Hutchings, B. Rainford, and H. Guggenheim, J. Phys. C: Solid State Phys. **3**, 307 (1970).

[74] D. E. Brown, T. Dumelow, T. J. Parker, K. Abraha, and D. R. Tilley, Phys. Rev. B **49**, 12266 (1994).

[75] R. E. Camley, Phys. Rev. Lett. **45**, 283 (1980).

[76] C. Cohen-Tannoudji, J. Dupont-Roc, and G. Grynberg, *Photons and Atoms-Introduction to Quantum Electrodynamics* (Wiley-VCH, Zurich, 1997), p. 486.

[77] P. A. M. Dirac, *The Principles of Quantum Mechanics* (Oxford University Press, Oxford, 1981), Vol. 27.

[78] R. J. Glauber and M. Lewenstein, Phys. Rev. A **43**, 467 (1991).

[79] L. D. Landau, J. Bell, M. Kearsley, L. Pitaevskii, E. Lifshitz, and J. Sykes, *Electrodynamics of Continuous Media* (Elsevier, Oxford, 2013), Vol. 8.

[80] A. Archambault, F. Marquier, J.-J. Greffet, and C. Arnold, Phys. Rev. B **82**, 035411 (2010).

[81] R. Matloob and R. Loudon, Phys. Rev. A **53**, 4567 (1996).

[82] R. Camley, Surf. Sci. Rep. **7**, 103 (1987).

[83] R. V. Mikhaylovskiy, T. J. Huisman, R. V. Pisarev, T. Rasing, and A. V. Kimel, Phys. Rev. Lett. **118**, 017205 (2017).

[84] K. Grishunin, T. Huisman, G. Li, E. Mishina, T. Rasing, A. V. Kimel, K. Zhang, Z. Jin, S. Cao, W. Ren *et al.*, ACS Photon. **5**, 1375 (2018).

[85] B. Cole, J. Williams, B. King, M. Sherwin, and C. Stanley, Nature (London) **410**, 60 (2001).

[86] R. Chikkaraddy, B. De Nijs, F. Benz, S. J. Barrow, O. A. Scherman, E. Rosta, A. Demetriadou, P. Fox, O. Hess, and J. J. Baumberg, Nature (London) **535**, 127 (2016).

[87] G. M. Akselrod, C. Argyropoulos, T. B. Hoang, C. Ciracì, C. Fang, J. Huang, D. R. Smith, and M. H. Mikkelsen, Nat. Photon. **8**, 835 (2014).

[88] J. Sloan, N. Rivera, M. Soljacic, and I. Kaminer, Nano Lett. **18**, 308 (2017).